Phase Transformations among TiO_2 Polymorphs

Miao Song, [‡, a] Zexi Lu, [‡, a] Dongsheng Li[*a]

[a] Physical and Computational Sciences Directorate, Pacific Northwest National Laboratory,

Richland, WA 99352, USA

[‡] The authors contribute equally

[*] Corresponding author: dongsheng.li2@pnnl.gov

1. Rutile identification

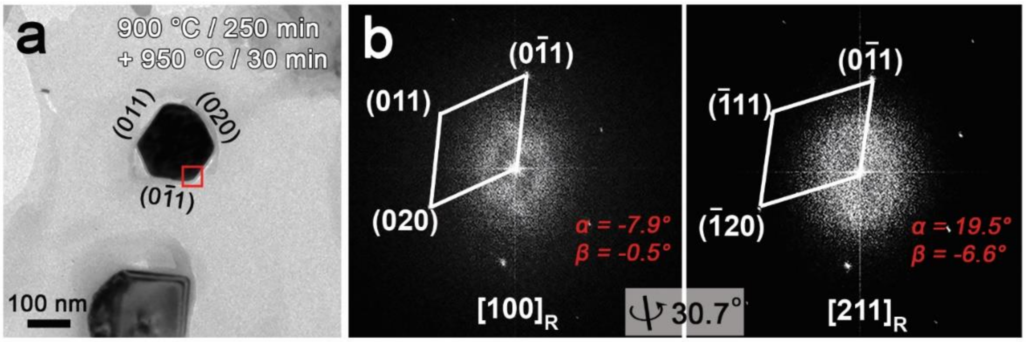

Fig. S1. Phase identification of rutile. (a) Bright-field (BF) image of the (001)-platelet in Fig. 1 after heating for 900°C 250 min + 950°C for 30 min. (b) Phase identification by tilting the particle in (a) to different zone axes. α and β are actual tilt angles of TEM holder. The theoretical tilt angle between the $[100]_R$ and $[211]_R$ is 30.7°, which is consistent with the experimental angle of 28.0° (from α = -7.9°, β= -0.5° to α = 19.5°, β= -6.6°)

2. Density functional theory (DFT) simulations

To investigate phase transformation pathways, we represented the initial (anatase) and final (rutile or brookite) structures using periodic cells of comparable sizes (Fig. 1e-i and Fig. 3e-i) with their orientations matching experimental observations (TEM diffraction patterns). For the anatase-to-rutile transformation (ART) pathway, 16 Ti atoms and 32 O atoms were in the simulation box and a gamma-centered 2 × 4 × 2 k-mesh was used. For the anatase-to-brookite transformation (ABT) pathway, 8 Ti atoms and 16 O atoms were in the simulation box and a gamma-centered 5 × 5 × 3 k-mesh was used. The optimized lattice parameters (Fig. 1i and Fig. 3i) differ by less than 3% from previously reported values (Table S2).

The transition path from anatase to the final structure was represented using transition steps t_a, t_b, and t_c, defined as:

$$t_\zeta = \frac{X_\zeta - X_{A,\zeta}}{X_{F,\zeta} - X_{A,\zeta}},\ 0 \le t_\zeta \le 1$$

Here, X_ζ is the reduced coordinate of Ti atoms along the ζ direction, where $\zeta = a, b,$ or c (lattice vectors). The A refers to anatase, and F refers to the final structure. The transformation was modeled by displacing the Ti atoms within the anatase unit cell toward their corresponding positions in the final unit cell. For the ART pathway, because the Ti relative positions along *a* direction remain almost unchanged (the difference is smaller than 1%), only two transition steps were introduced along this direction (t_a=0 and 1). Both the other two directions had five transition steps with an interval of Δ*t*=0.25, resulting in a total of 50 possible intermediate structures. To pinpoint the most preferable transition pathway, all possible structures with different (t_a, t_b, t_c) combinations were tested. Each structure was optimized using self-consistent static calculations with all Ti atoms fixed, and all O atoms and the cell relaxed. The most preferable path (Fig. 1j) was then determined from the cell energy contour (Fig. 1k), along which there is a minimum energy barrier. The same procedure was done for the ABT pathway, except that five transition steps were introduced for each of all three lattice vectors, resulting in a total of 125 possible intermediate structures. The optimal pathway and energy contour are shown in Fig. 3j and 3k. Fig. S2 is the evolution of lattice parameters along different paths during the DFT simulated ART and ABT processes.

The e-beam sputtering process was quantified by calculating the displacement energy of O atoms along the e-beam directions using DFT. In each calculation, one O atom in an otherwise pristine periodic anatase primitive cell was displaced by 0.2 Å along the e-beam direction. All atoms and the cell dimensions were fixed for a single-point energy calculation. The displacement energy (unit: eV/Å) was then defined as the difference in free energies between the displaced and pristine unit cells, normalized by the displacement of 0.2 Å. These calculations were performed for every O atom in the anatase primitive cell with respect to all three e-beam directions ($[010]_A$, $[101]_A$ and $[111]_A$). The displacement energies with respect to different O atoms and e-beam orientations are shown in Fig. 5m and 5n.

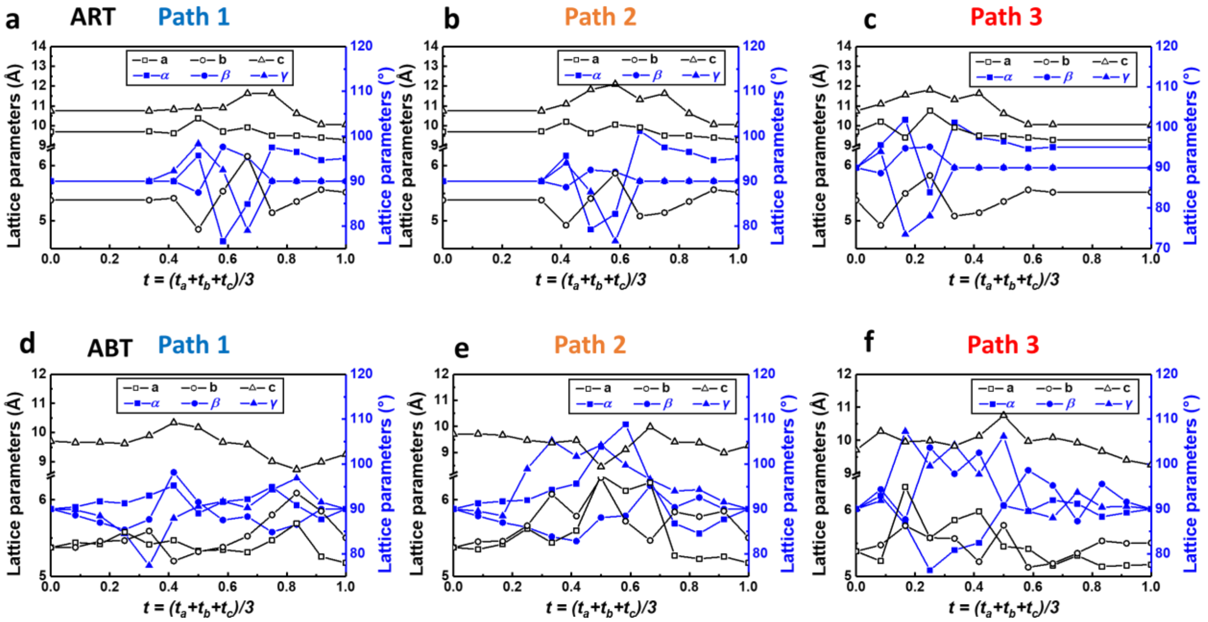

Fig. S2 Evolution of lattice parameters of the paths 1, 2, and 3 during the DFT simulated ART (a-c) and ABT (d-f) processes.

3. Another ART process identified by *in situ* selected area electron diffraction (SAED) TEM experiment

To study the details of structural evolution during the ART process, we tracked another platelet particle during, instead of before and after, the heating process via an *in situ* heating experiment. To avoid the e-beam effect at high temperature, an *in situ* SAED experiment was carried out at 950°C (see also details in Methods). Multiple sets of diffraction patterns in the SAED pattern from the sample after heating for 7 min (Fig. S3b) show that the original $[001]_A$ single crystal (Fig. S3b 0 min) evolved into a polycrystal, indicating that many nuclei with various orientations formed simultaneously in the original anatase single crystal. The polycrystals transferred into a nearly single crystal at 54 min (an intermediated phase, Fig. S3b 54 min) and then polycrystal again (Fig. S3b 78 min, 100 min). After 100 min, the crystal is in a mixed phase of rutile and B phase. The rutile structure was verified by tilting the particles to different zone axes in Fig. S3d, confirming the ART of the relationship of $[001]_A \parallel [11\bar{2}]_R$, $(020)_A \parallel (1\bar{1}0)_R$. As shown in Fig. S3e, $[\bar{1}\bar{1}0]_A$ can be acquired by rotating $[001]_A$ 90.0° in plane of $(\bar{1}10)_A$ and $[0\bar{1}\bar{1}]_R$ can be acquired by rotating $[11\bar{2}]_R$ 94.3° in plane of$(3\bar{1}1)_R$, respectively. Therefore, this ART orientation relationship is also equivalent to $\langle 110\rangle_A || \langle 011\rangle_R$, $\{112\}_A || \{200\}_R$, which was reported previously via postmortem experiments [1]. Notably, various ART orientation relationships and the appearance of polycrystal and some intermediate phases during the phase transformation process verified that the ART process is complicated; that is, this process involves various intermediate phases and evolution pathways instead of the direct transformation from one phase to another phase trigged by one nucleus.

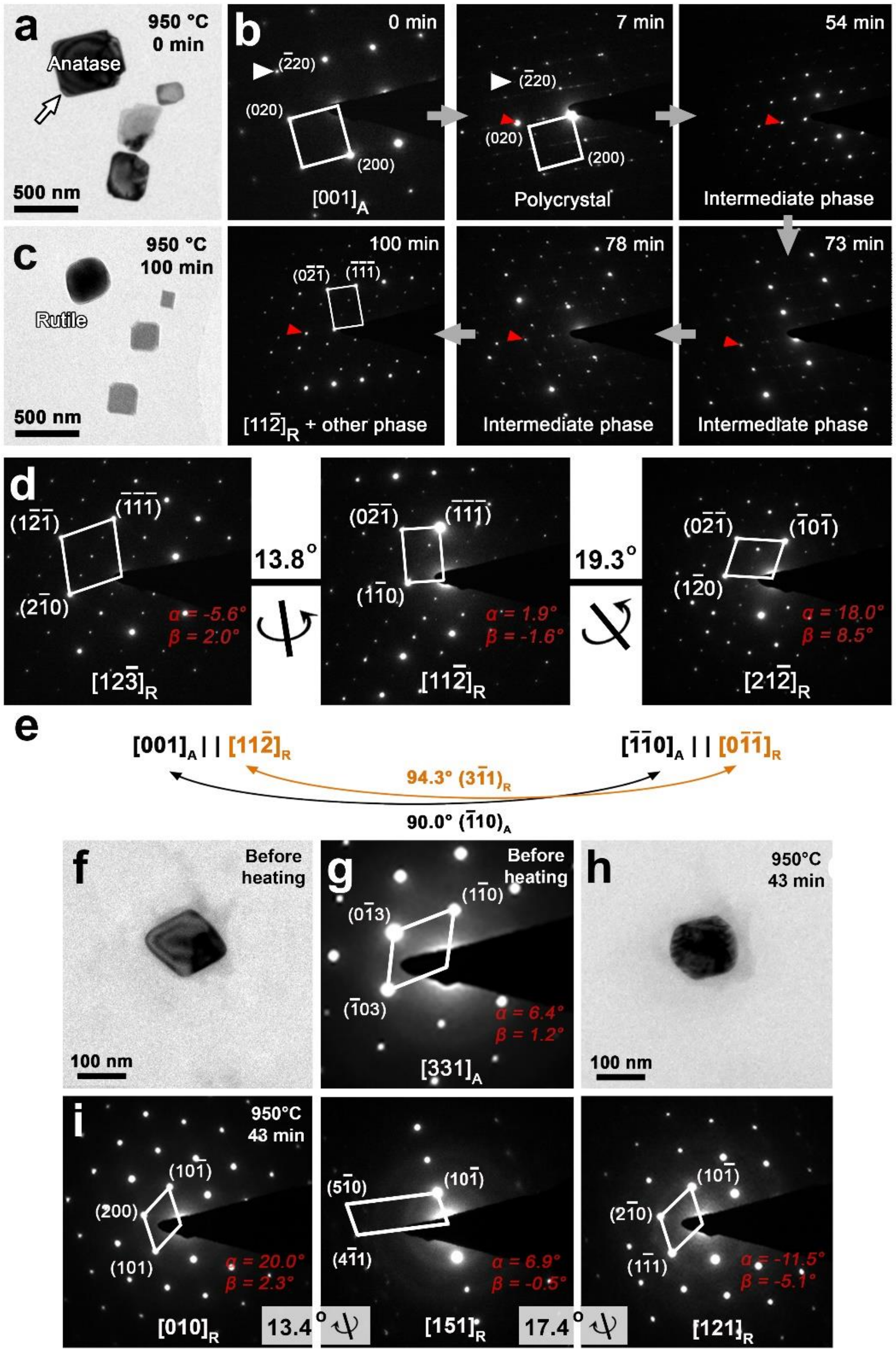

Fig. S3. Two examples of phase transformation from anatase to rutile. (a-e) ART via the $[001]_A \parallel [11\bar{2}]_R$, $(\bar{2}00)_A \parallel (\bar{1}\bar{1}\bar{1})_R$ pathway. (a) and (c) BF images showing the morphology evolution of a (001)-platelet (denoted by the white arrow) before and after heating at 950°C for 100 min. (b) Time-sequenced *in situ* SAED patterns of the particle in (a) showing the phase transformation from anatase to B phase and rutile. Diffraction spots denoted by the same red arrows were used for tracking phase evolution during the heating process. (d) Rutile identification by tilting the particle in (c) to different zone axes. α and β are actual tilt angles of the TEM holder. The theoretical tilt angles between the $[12\bar{3}]_R$ and $[11\bar{2}]_R$, $[11\bar{2}]_R$ and $[21\bar{2}]_R$ are 13.8° and 19.3°, consistent with the experimental angle of 8.3°, and 18.9°, respectively. (e) Demonstration of equivalent ART orientation relationships of the observed $[001]_A \parallel [11\bar{2}]_R$ with previously reported $[110]_A \parallel [011]_R$ [1]. For example, $[001]_A$ zone axis can be obtained by tilting $[110]_A$ in $(\bar{1}10)_A$ plane for 90° and $[11\bar{2}]_R$ can be obtained by tilting $[011]_R$ in $(3\bar{1}1)_R$ for 94.3°. (f-i) Another example of phase transformation from anatase to rutile. (f) and (h) BF images of an octahedral nanoparticle before and after *in situ* heating. (g) SAED pattern of the particle in (f). (i) SAED patterns of different zone axes of the particle in (h) verifying that anatase has transformed into rutile after *in situ* heating at 950°C for 43 min. The theoretical tilt angle between $[010]_R$ and $[151]_R$ is 13.4°, and that between $[151]_R$ and $[121]_R$ is 17.4°, consistent with experimental angles of 13.4° and 19.0°, respectively.

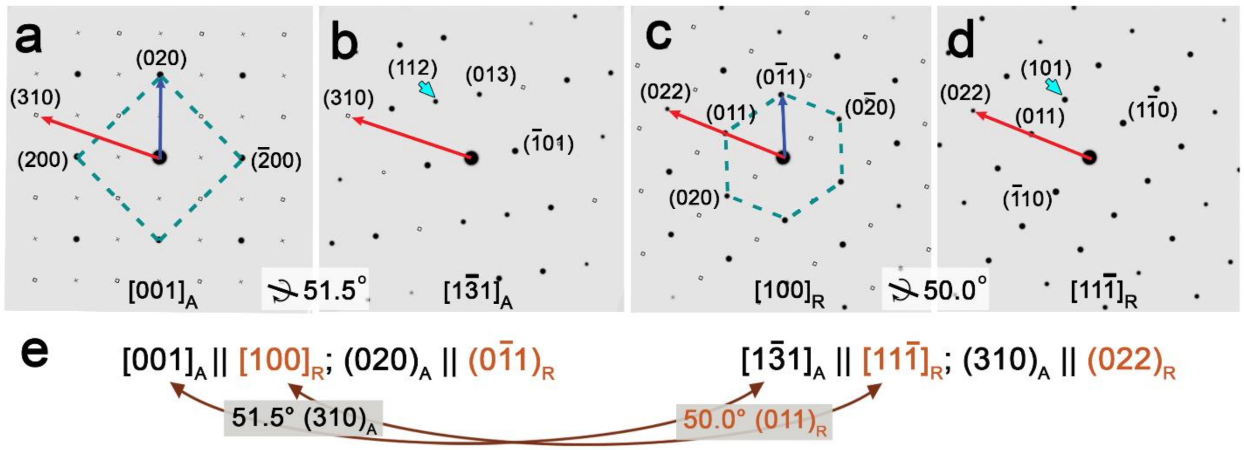

Fig. S4. Equivalent ART relationship. (a–d) Simulated diffraction patterns of $[001]_A$, $[1\bar{3}1]_A$, $[100]_R$, and $[11\bar{1}]_R$, respectively. The tilt angle from $[001]_A$ to $[1\bar{3}1]_A$ is 51.5° with a co-plane of $(310)_A$. The tilt angle from $[100]_R$ to $[11\bar{1}]_R$ is 50.0° with a co-plane of $(022)_R$. The common twin interfaces of $[112]_A$ and $[101]_R$ are denoted by the cyan arrows in (b) and (d), respectively. (e) Equivalent ART orientation relationships presented from (a) to (b) and (c) to (d).

4. ABT phase transformation

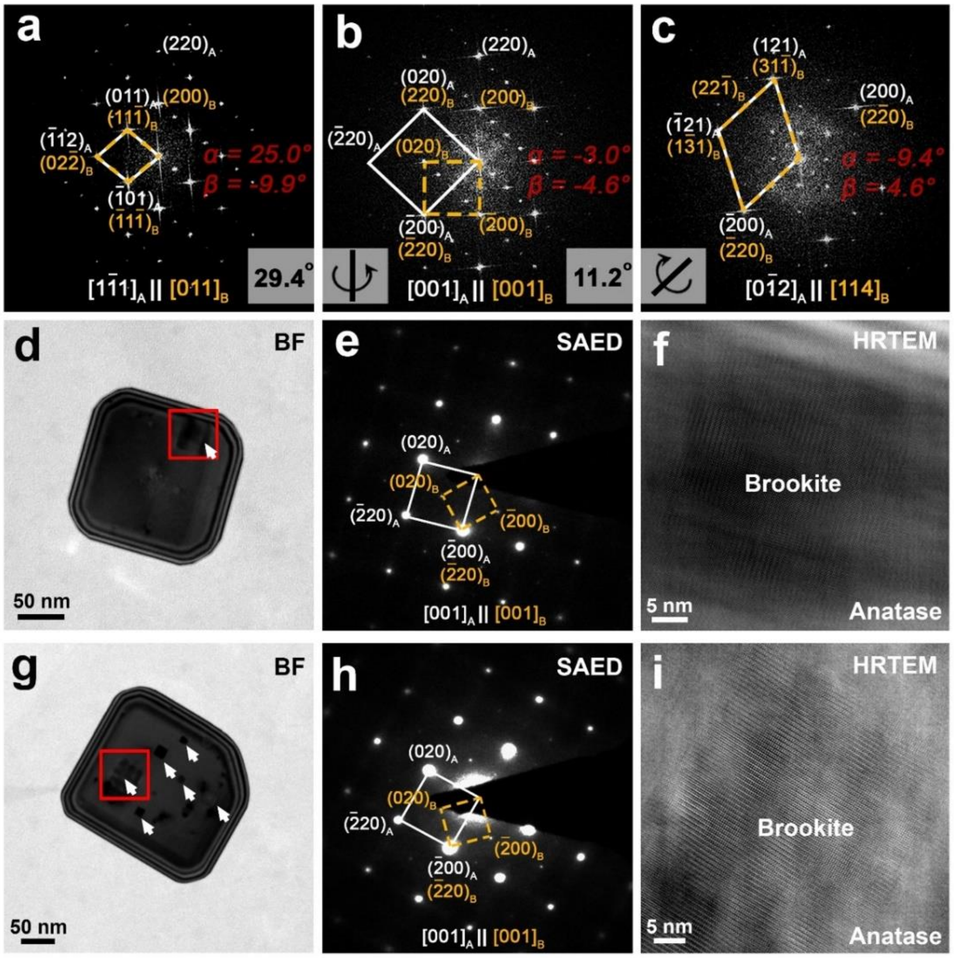

Fig. S5. Identification of phase transformation relationship between anatase and brookite and other examples showing the brookite phase embedded in anatase (001) platelet. (a–c) Fast Fourier transform (FFT) images of the red-boxed area in Fig. 3b by tilting the particle to different zone axes verifying that anatase has partially transformed into brookite. The theoretical tilt angles of anatase of 29.4° ($[1\bar{1}1]_A$ and $[001]_A$) and 11.2° ($[001]_A$ and $[0\bar{1}2]_A$) are close to that of brookite of 30.7° ($[011]_B$ and $[001]_B$) and 11.5° ($[001]_B$ and $[114]_B$), respectively. α and β are actual tilt angles of the TEM holder. The remnant diffraction spots in (d) result from the overlap of anatase and brookite phases. (d) and (g) TEM-BF images showing the brookite phase embedded in (001) platelets after heating at 1000°C for 20 min. The brookite phase is denoted by white arrows. (e) and (h) SAED patterns of the particles in (d) and (g), respectively, verifying the ABT orientation relationship of $[001]_A \parallel [001]_B$, $(020)_A \parallel (220)_B$. (f) and (i) High-resolution transmission electron microscopy (HRTEM) images of red-boxed areas in (d) and (g), respectively.

5. E-beam induced phase transformation from anatase to R-phase and R-phase back to anatase at high temperature

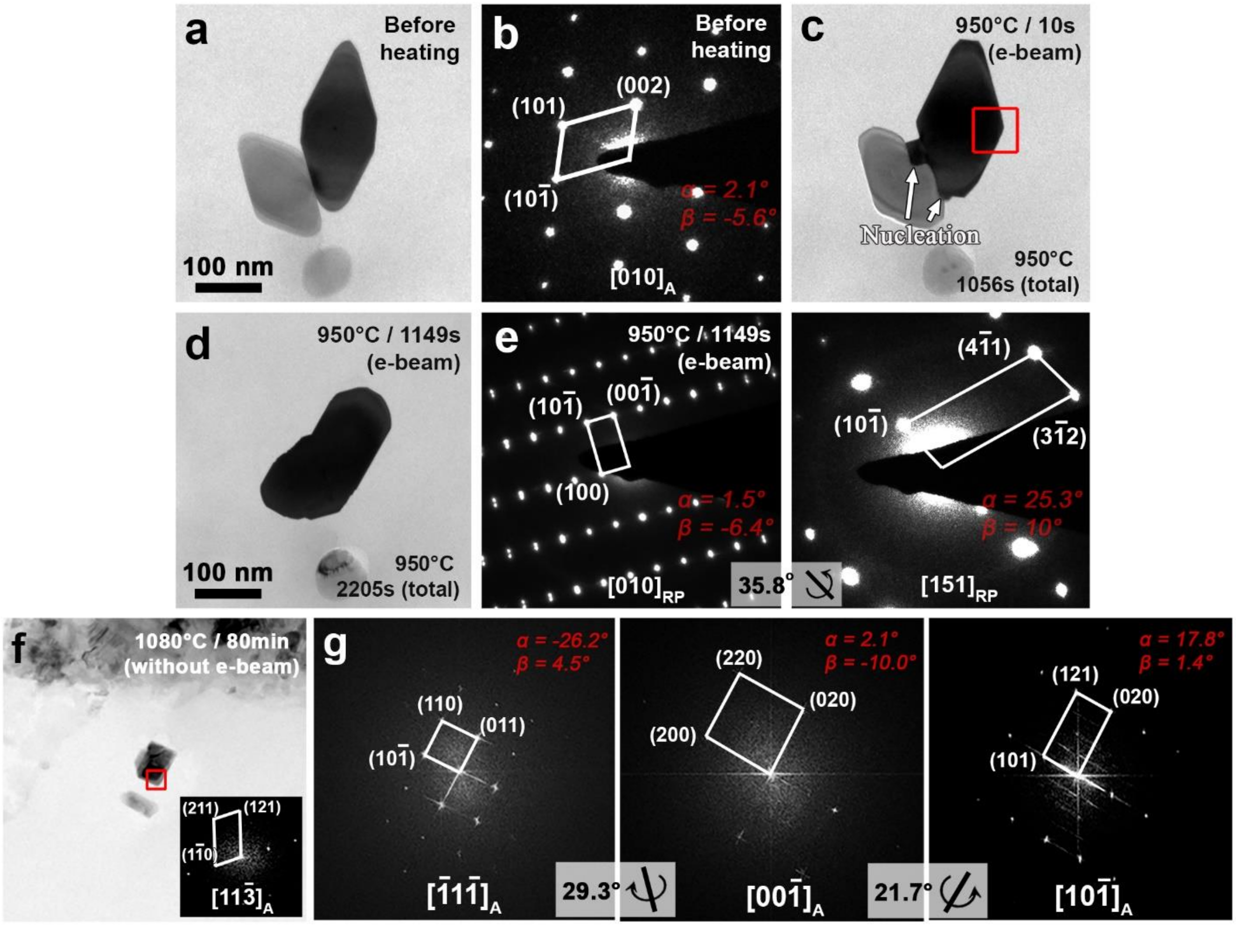

Fig. S6. The phase transformation from anatase to R-phase (RP) and back to anatase**.** (a) and (b) BF image and SAED pattern showing the original morphology and orientation of octahedral nanoparticles before heating. (c) Nucleation of RP at particle interfaces (denoted by white arrows) under e-beam with a dose rate of ~3.0 × 10^4 e·nm^{-2}·s^{-1} at 950°C. (d) BF image showing morphology evolution after heating at 950°C for 1149 s under e-beam. (e) Phase identification by tilting the particle to various zone axes. The theoretical angle between $[010]_{RP}$ and $[151]_{RP}$ is 35.8°. (f) BF image and FFT DP (inset) of another particle (Fig. 4d-f) that is transformed from anatase to R-phase, and back to anatase phase after heating at 1080°C. (g) FFT DPs of the red-boxed area in (f) by tilting the particle to various zone axes, confirming the anatase phase. The theoretical angle is 35.8° between $[\bar{1}1\bar{1}]_A$ and $[00\bar{1}]_A$, and 21.7° between $[00\bar{1}]_A$ and $[10\bar{1}]_A$, consistent with experimental angles of 31.4° (β reached the largest tilt angle of the TEM holder, 10°) and 22.8°, respectively. α and β are actual tilt angles of the TEM holder.

6. E-beam induced reduction of TiO_2 to TiO

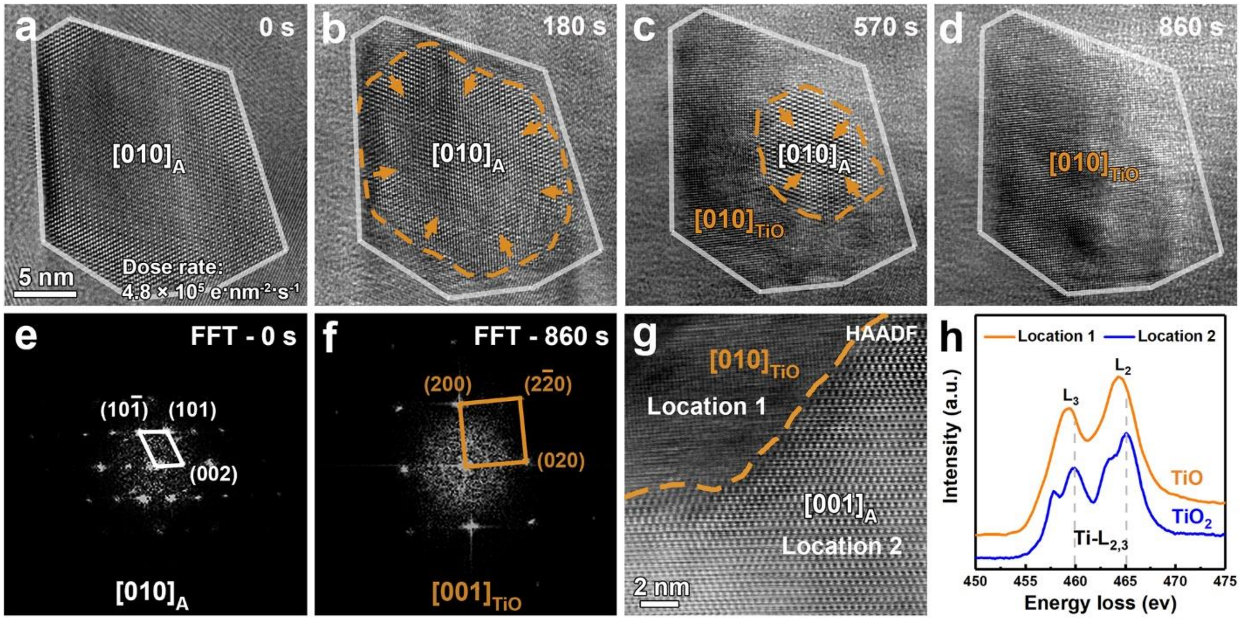

Fig. S7. E-beam induced phase transformation from anatase to TiO at room temperature. (a–d) Time-sequenced in situ HRTEM images showing the phase transformation from anatase to TiO. The edges of the original anatase particle are outlined by white lines. The interface between anatase and TiO is denoted by yellow dashed lines. (e) and (f) FFT DPs of 0 s and 860 s, respectively, verifying that the original anatase transformed into TiO with the orientation relationship of $[010]_A \parallel [010]_{TiO}$, $(002)_A \parallel (020)_{TiO}$. (g) High-angle annular dark-field (HAADF) image of an e-beam induced phase transformation region. (h) electron energy loss spectra of locations 1 and 2 in (g) verifying that the e-beam induced phase is TiO.

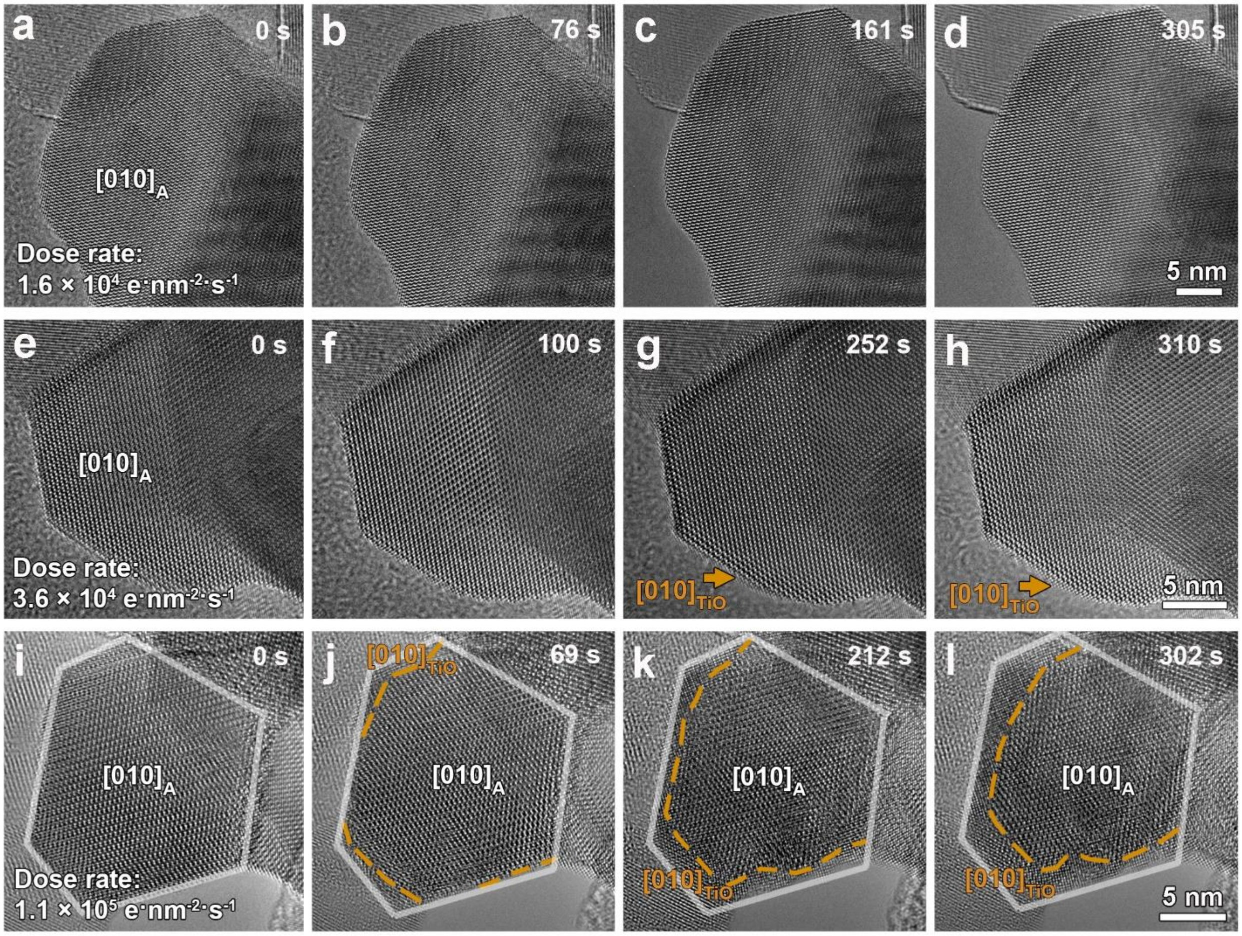

Fig. S8. E-beam induced reduction of anatase-$[010]_A$ to TiO at room temperature under irradiation with various e-beam intensities. (a–d) 1.6 ×10^4 e·nm^{-2}·s^{-1}, (e-h) 3.6×10^4 e·nm^{-2}·s^{-1}, and (i–l) 1.1×10^5 e·nm^{-2}·s^{-1}. The critical dose rate is ~4 × 10^4 e·nm^{-2}·s^{-1} above which the TiO_2 tends to be reduced by e-beam. The edges of the original anatase particle in (i–l) are outlined by white lines. The interface between anatase and TiO in (j–l) are denoted by yellow dashed lines. The phase transformation directions are denoted by yellow arrows.

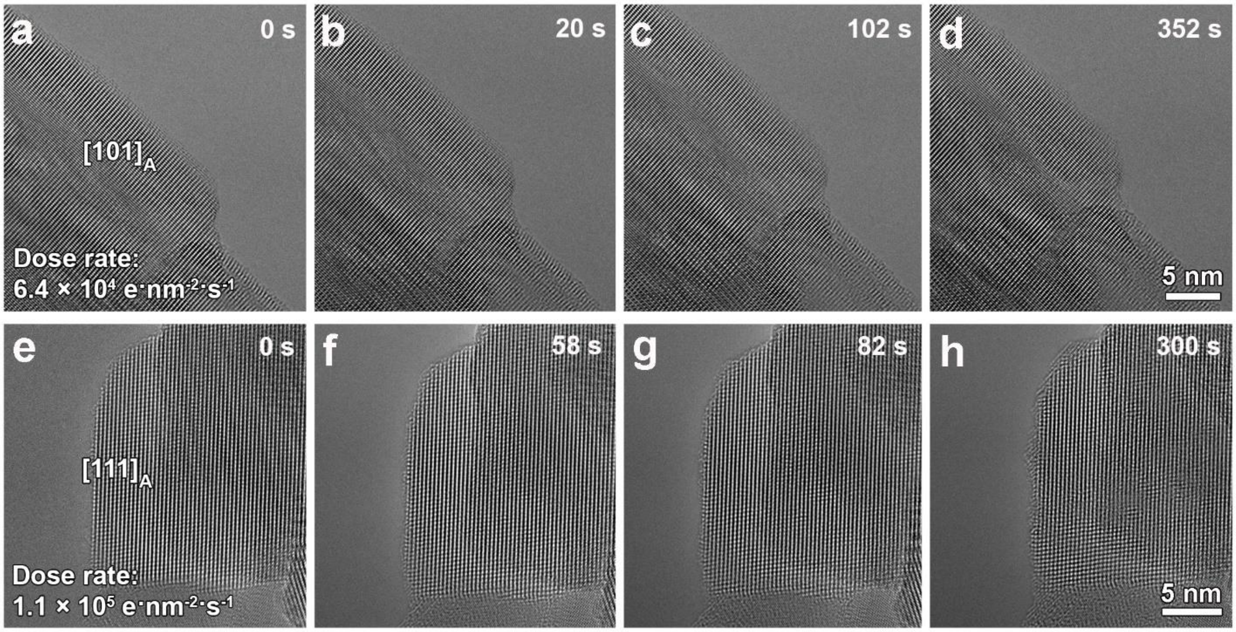

Fig. S9. More examples of e-beam effect on [101] and [111] anatase orientations at room temperature. (a–d) An example of $[101]_A$ nanoparticles under irradiation of e-beam with a dose rate of 6.4 ×10^4 e·nm^{-2}·s^{-1}. (e-h) An example of $[111]_A$ nanoparticles under irradiation of e-beam with a dose rate of 1.1 ×10^5 e·nm^{-2}·s^{-1}. No obvious structure variations were observed, unlike $[010]_A$ in Fig. 6a-d and Fig. S8i–l. Dose rates employed here are larger than the critical dose rate of ~4×10^4 e·nm^{-2}·s^{-1} employed for the redox reactions from TiO_2-$[010]_A$ to TiO.

7. The need for in situ TEM investigation

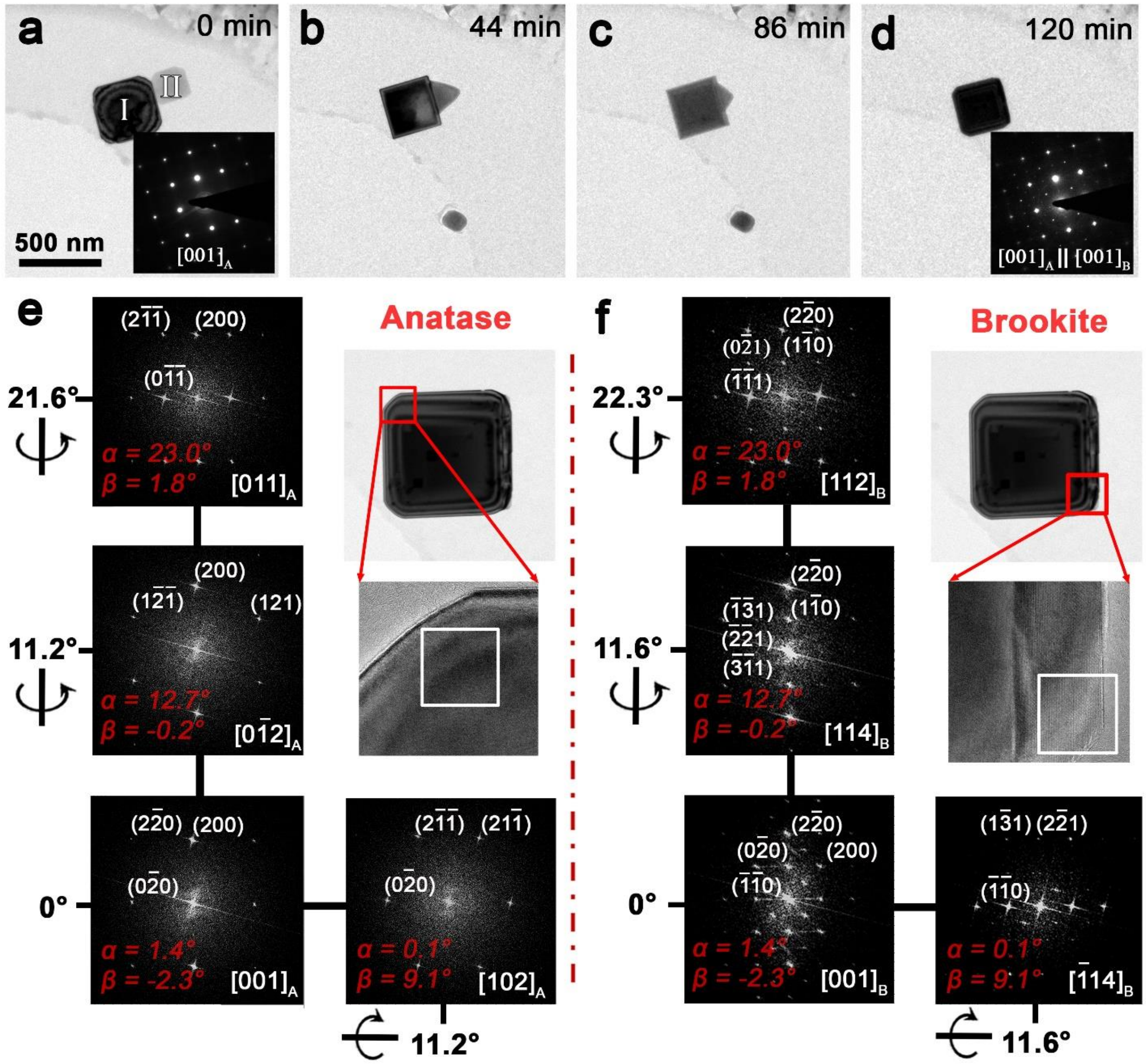

Fig. S10. Possible ABT orientation relationship of $[001]_A \| [001]_B$, $(020)_A \| (220)_B$. (a–d) Time-sequenced BF images showing morphology evolution at 950°C. Insets are corresponding SAEDs. (e) Anatase phase identification via FFT DPs (white-boxed area) obtained by tilting the particle in (d) to various zone axes. (f) Brookite identification via FFT DPs of the white-boxed area obtained at corresponding tilt angles in (e). α and β are actual tilt angles of the TEM holder.

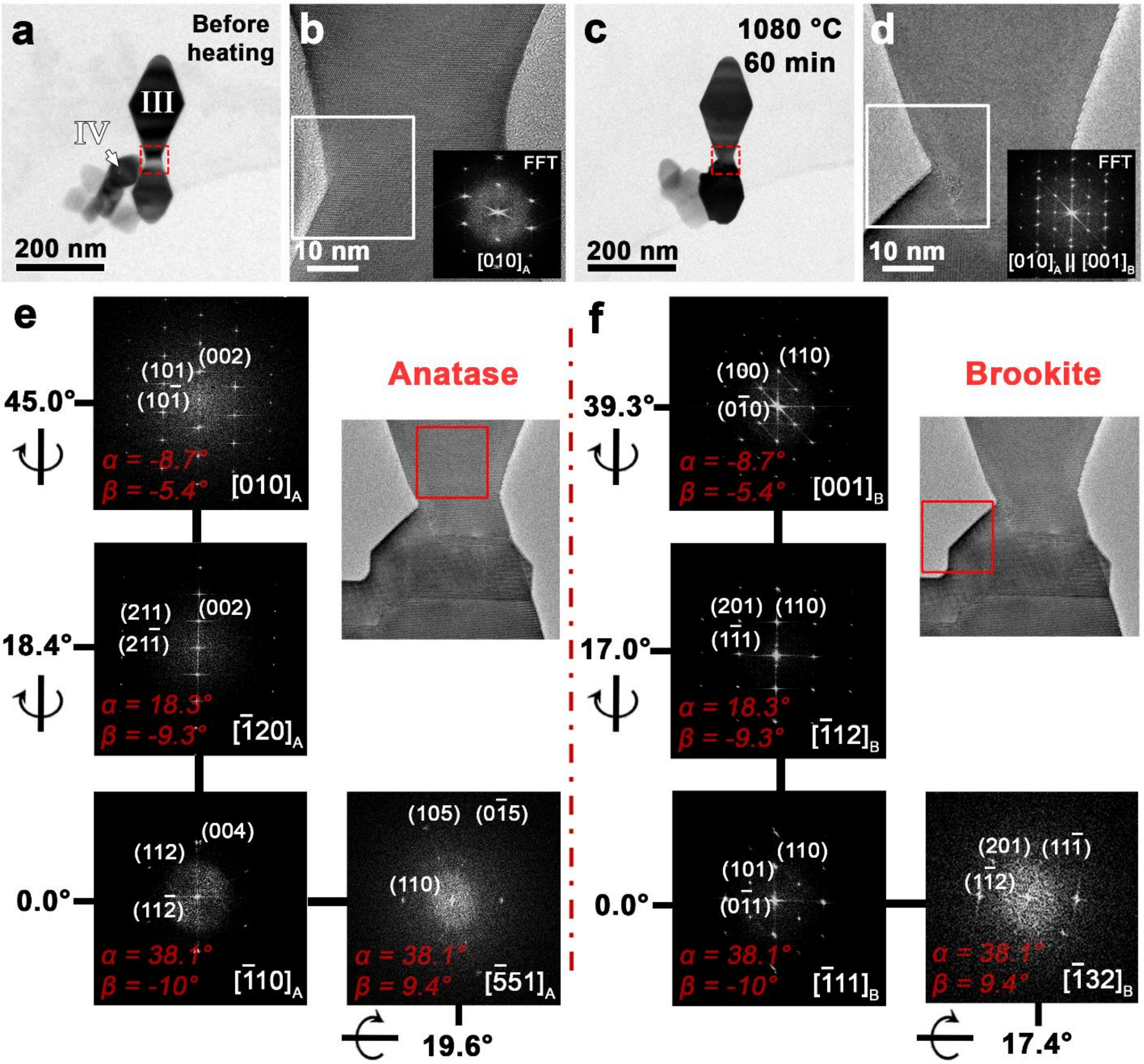

Fig. S11. Possible ABT orientation relationship of $[010]_A \parallel [001]_B$; $(002)_A \parallel (110)_B$. (a) and (c) BF images of octahedral nanoparticles before and after heating at 1080°C for 60 min. (b) and (d) HRTEM images of the red-boxed areas in (a) and (c), respectively. Insets are corresponding FFT DPs of the white-boxed areas in (b) and (d). (e) and (f) Phase identifications of red-boxed areas by tilting the particle to various zone axes. α and β are actual tilt angles of the TEM holder.

8. Morphologies of various anatase nanoparticles

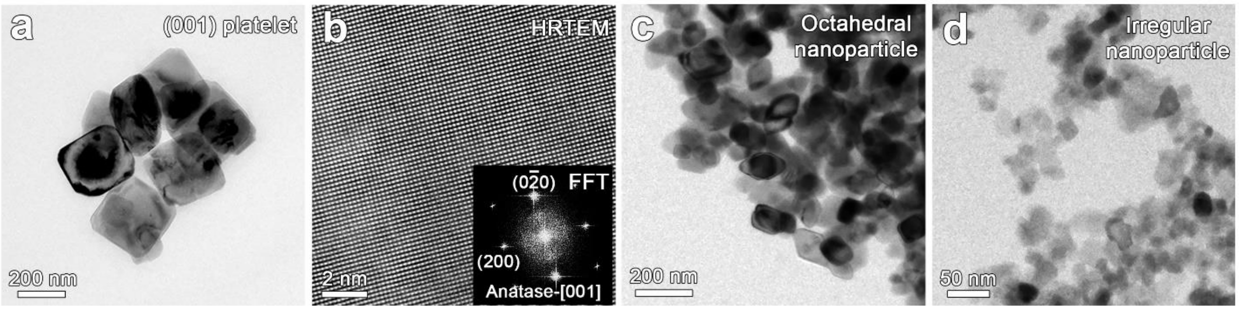

Fig. S12. Morphologies of various anatase nanoparticles. (a) {001}-platelet with an average particle size of ~270 nm. (b) HRTEM image of a (001)-platelet. The inset is the FFT from the HRTEM image. (c) Octahedral nanoparticles with an average particle size of ~82 nm. (d) Irregular nanoparticles with an average particle size of ~23 nm.

9. Experimental procedures

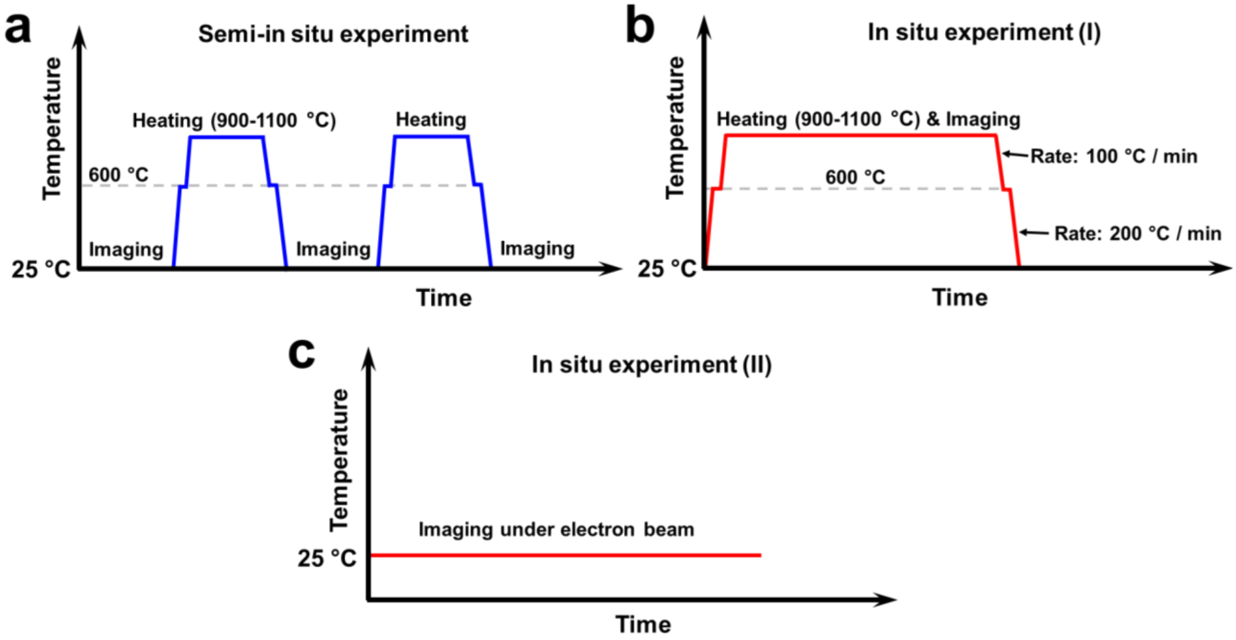

Fig. S13. Schematic illustration of heating and imaging procedures. (a) Semi-*in situ* experiments were realized by imaging at room temperature and heating at high temperatures (900–1100 °C) mainly for the ART and ABT processes. (b) *In situ* experiment (I) realized by heating and imaging at high temperatures for the ART. For the transformation from anatase to TiO_2-B, a low electron dose rate (~50 e·nm^{-2}·s^{-1}) under SAED mode was used. For the transformation from anatase to R-phase, a high dose rate (~10^{4} e·nm^{-2}·s^{-1}) under BF imaging mode was used. (c) *In situ* experiment (II) realized by imaging at room temperatures under a high dose rate (>~4×10^{4} e·nm^{-2}·s^{-1}) for the phase transformation from anatase to TiO.

10. METHODS

Material synthesis. Anatase nanoparticles with three different morphologies were employed in the experiment, including {001}-platelets (Fig. S12a-b), octahedrons (Fig. S12c), and irregular shapes (Fig. S12d). Octahedral particle and (001) platelet were synthesized according to previous reports of gas-phase reaction process [2] and hydro-thermal method [3], respectively. Anatase nanoparticles with irregular shapes were synthesized by a hydrosolvothermal method. At first, 180 µL of titanium (IV) tetrabutoxide and 1.63 g of DL-histidine were dissolved in a mixture of 8 mL H_2O and 2 mL of a 37 % solution of hydrochloric acid (HCl). The prepared solution was transferred into a sealed 23 mL Teflon-lined autoclave and held at 150 °C over 3.5 h. All chemicals including titanium (IV) butoxide (97 %, Sigma-Aldrich), DL-histidine (>98 %, TCI), and HCl (37 %, Sigma-Aldrich) were used as received.

(Semi) *in situ* heating experiment. The phase transformation activation energy of a single anatase nanoparticle is significantly higher than that of aggregated anatase particles [4]. For example, aggregated anatase particles transform into rutile at the temperature of ~700^{o}C, while the individual small anatase particles could be stable up to 1000 °C [5]. In our experiment, a high temperature (900-1100 ºC) was used for the phase transformation. To avoid/minimize electron-beam (e-beam) effects, which will be magnified at high temperatures (900-1100 ºC), we first conducted semi *in situ* heating experiments (Fig. S13a), in which the temperature was increased to 900-1100 °C for phase transformation and lowered to room temperature during imaging. The samples were only exposed under the electron beam at room temperature. The effect of e-beam at room temperature during imaging was also studied for the phase transformation. We chose the electron dose rate ($<\sim 10^4$ $e \cdot nm^{-2} \cdot s^{-1}$) that does not show an obvious effect. During this process, to avoid membrane breaking due to sudden temperature change, the temperature was first increased to 600 °C (heating rate: 200 °C/min) and stabilized for ~10 min, then ramped to targeted temperature (900-1100 ºC) at a rate of 100 °C/min and held at these temperatures for different durations. After the heating process, the temperature was decreased to 600 °C first at a rate of 100 °C/min and then to room temperature at a rate of 200 °C/min. We also conducted in situ TEM experiments, in which, to reduce e-beam effects, we only took selected area electron diffraction (SAED) to analyze the structural evolution of crystals due to the extremely low electron dose rate at SAED mode (~ 50 $e^{-}·nm^{-2}·s^{-1}$) in contrast to HRTEM imaging mode (~1-5 × 10^4 $e^{-}·nm^{-2}·s^{-1}$). Typically, the same exposure time of 0.5 s and image size of 1024 pixels ×1024 pixels were employed during SAED and HRTEM imaging processes.

Two different types of SiNx heating chips were used in our experiments. One is the older design, which has 49 (7×7) holes with a variation of ~160°C over ~100 μm [6] and the other one is the newer design, which has 9 (3×3) holes with a variation of ~20ºC over ~ 30 μm. Based on numerous experiments, we estimated the temperature for the phase transformation from anatase to rutile ranges from 900 to 1000 ºC. Therefore, it was difficult for us to predict the exact temperature for the phase transformation to take place for each particle on the heating chip. To track the whole process of phase transformation, we started to image the particles at ~900ºC and then increased the temperature little by little if phase transformation did not happen.

E-beam effects and e-beam induced phase transformation were also studied. *In situ* TEM experiments were employed to observe the e-beam induced phase transformation at high temperatures (>900 ºC, Fig. S13b) and room temperature (Fig. S13c). We found that continuously (e.g., tens of seconds) exposing the sample under e-beam (> ~3 × 10^4 $e^{-}·nm^{-2}·s^{-1}$) at a high temperature of 900-1100 ºC induced the phase transformation from anatase into R-phase TiO_2 instead of rutile or brookite. Crystal structures of various phases evolved in our experiment are presented in Table S2.

Microstructure characterization. An aberration-corrected environmental transmission electron microscope (ETEM, Thermo Fisher Scientific, USA) was employed at 300 kV for bright-field (BF) images, SAED, and high-resolution TEM (HRTEM) images. *In situ* and semi-*in-situ* heating experiments were performed using a Protochips Aduro double tilt heating holder with a tilting angle range of $\alpha = \pm 30°$, $\beta = \pm 10°$, enabling orientation relationship analysis during/after the heating process by tilting samples to different zone axes. Protochips thermal E-chips (E-AHBC) were used in our experiments. The heating part is composed of a ceramic membrane heating element coated with a thin amorphous carbon film. Sample tilting angles were denoted in Figures, or else there was no sample tilt during the experiment. Temperatures in the experiment were read on Protochips Aduro software and were calibrated for each chip by holder and chip provider. The chip and sample temperature might vary a little. A single anatase particle could maintain its crystal unchanged under 800 °C for less than 60 min in the experiment.

For phase identification, we tilted samples to various zone axes. Generally, to acquire an accurate HRTEM image, the theoretical largest tolerant deviation angle from the perfect zone axis should be less than 2.5° perpendicular to the symmetrical diffraction spots direction (i.e., separated/clear crystal plan) for crystals thicker than 20 nm [7, 8]. In actual experiments, the deviation angle of each FFT images might be slightly larger than 2.5° due to the overlapping of crystals or the limited tilting angle of β = ± 10. We estimate that we had ~5° deviation from the perfect zone axis in our HRTEM acquiring experiments, resulting in the actual tilting angle between two zone axes possibly slightly different from the theoretical angles.

Density functional theory simulations. All DFT simulations were performed using the Vienna ab initio Simulation Package (VASP) [9, 10]. The core electrons ($1s^22s^22p^6$ for Ti, $1s^2$ for O) were represented by projector augmented-wave pseudopotentials [11, 12]; the standard generalized gradient approximation Perdew-Burke-Ernzerhof exchange correlation functional was used [13]. The energy cutoff of 600 eV was used throughout all calculations, and the threshold for self-consistent field convergence was set to 10^{-6} eV.

Table S1. Reported orientation relationships among various TiO_2 polymorphs

Orientation relationship between anatase and rutile	Orientation relationship between anatase and brookite
$\langle 010\rangle_A \Vert \langle 110\rangle_R, \{112\}_A \Vert \{010\}_R$ [14]	$\langle 131\rangle_A \Vert \langle 011\rangle_B, \{112\}_A \Vert \{100\}_B$ [17]
$\langle 110\rangle_A \Vert \langle 011\rangle_R, \{112\}_A \Vert \{200\}_R$ [15]	$\langle 110\rangle_A \Vert \langle 001\rangle_B, \{002\}_A \Vert \{200\}_B$ [18]
$\langle 201\rangle_A \Vert \langle 111\rangle_R, \{101\}_A \Vert \{101\}_R$ [16]	

Table S2. Crystal structures of various phases.

Phase	Space group	Lattice parameter					
		a (Å)	b (Å)	c (Å)	α (°)	β (°)	γ (°)

Anatase [19]	I4$_1$/amd	3.784	3.784	9.515	90.0	90.0	90.0
Rutile [19]	P4$_2$/mnm	4.593	4.593	2.959	90.0	90.0	90.0
Brookite [19]	Pbca	5.163	5.439	9.519	90.0	90.0	90.0
B phase [20]	C2/m	12.179	3.741	6.525	90.0	107.05	90.0
RP [21]	I4/m	9.459	2.958	4.902	90.0	90.0	90.0
TiO [22]	Fm-3m	4.177	4.177	4.177	90.0	90.0	90.0

References

1. P. I. Gouma and M. J. Mills, *J. Am. Ceram. Soc.*, 2001, **84**, 619-622.
2. F. Amano, O.O. Prieto-Mahaney, Y. Terada, T. Yasumoto, T. Shibayama and B. Ohtani, *Chem. Mater.*, 2009, **21**, 2601-2603.
3. C. Chen, R. Hu, K. Mai, Z. Ren, H. Wang, G. Qian and Z. Wang, *Cryst. Growth Des.*, 2011, **11**, 5221-5226.
4. H. Zhang and F. Banfield Jillian, *Am. Mineral.*, 1999, **84**, 528.
5. W. Dong, Y. Sun, C. W. Lee, W. Hua, X. Lu, Y. Shi, S. Zhang, J. Chen and D. Zhao, *J. Am. Chem. Soc.,* 2007, **129**, 13894-13904.
6. M. Picher, S. Mazzucco, S. Blankenship and R. Sharma, *Ultramicroscopy*, 2015, **150**, 10-15.
7. Z. Xiaodong, F. Embaie A and H. Sven, *Phys. Chem. Miner.*, 1995, **22**, 517-523.
8. S. Hovmöller and Z. Xiaodong, *Microsc. Res. Tech.*, 1999, **46**, 147-159.
9. G. Kresse and J. Hafner, *Phys. Rev. B*, 1993, **47**, 558-561.
10. G. Kresse and J. Furthmüller, *Comp. Mat. Sci.*, 1996, **6**, 15-50.
11. P. E. Blöchl, *Phys. Rev. B*, 1994, **50**, 17953-17979.
12. G. Kresse and D. Joubert, *Phys. Rev. B*, 1999, **59**, 1758-1775.
13. J. P. Perdew, K. Burke and M. Ernzerhof, *Phys. Rev. Lett.*, 1996, **77**, 3865-3868.
14. R. L. Penn and F. Banfield Jillian, *Am. Mineral.*, 1999, **84**, 871-876.
15. P. I. Gouma and M. J. Mills, *J. Am. Ceram. Soc.*, 2001, **84**, 619-622.
16. Y. Shao, D. Tang, J. Sun, Y. Lee and W. Xiong, *China Particuology*, 2004, **2**, 119-123.
17. R. L. Penn and J. F. Banfield, *Am. Mineral.*,1998, **83**, 1077-1082.
18. A. Lotnyk, S. Senz and D. Hesse, *Thin Solid Films*, 2007, **515**, 3439-3447.
19. D.W. Kim, N. Enomoto, Z.e. Nakagawa and K. Kawamura, *J. Am. Ceram. Soc.*, 1996, **79**, 1095-1099.
20. T. P. Feist and P. K. Davies, *J. Solid State Chem.*, 1992, **101**, 275-295.
21. J. Akimoto, Y. Gotoh, Y. Oosawa, N. Nonose, T. Kumagai, K. Aoki and H. Takei, *J. Solid State Chem.*, 1994, **113**, 27-36.
22. A. NoÊRlund Christensen, *Acta chem. scand. (1989)*, 1990, **44**, 851-852.